A&A, 685, A98 (2024)
https://doi.org/10.1051/0004-6361/202349019

Astronomy & Astrophysics

The miniJPAS survey

Optical detection of galaxy clusters with PZWav*

L. Doubrawa[1,2], E. S. Cypriano[2], A. Finoguenov[1], P. A. A. Lopes[3], A. H. Gonzalez[4], M. Maturi[5,6], R. A. Dupke[7,8,9], R. M. González Delgado[10], R. Abramo[11], N. Benitez[10], S. Bonoli[12,13,14], S. Carneiro[15], J. Cenarro[12], D. Cristóbal-Hornillos[12], A. Ederoclite[12], A. Hernán-Caballero[12], C. López-Sanjuan[12], A. Marín-Franch[12], C. Mendes de Oliveira[2], M. Moles[12], L. Sodré Jr.[2], K. Taylor[16], J. Varela[12], and H. Vázquez Ramió[12]

(Affiliations can be found after the references)

Received 19 December 2023 / Accepted 14 February 2024

ABSTRACT

Context. Galaxy clusters are an essential tool to understand and constrain the cosmological parameters of our universe. Thanks to its multi-band design, J-PAS offers a unique group and cluster detection window using precise photometric redshifts and sufficient depths.
Aims. We produced galaxy cluster catalogues from miniJPAS, which is a pathfinder survey for the wider J-PAS survey, using the PZWav algorithm.
Methods. Relying only on photometric information, we provide optical mass tracers for the identified clusters, including richness, optical luminosity, and stellar mass. By reanalysing the *Chandra* mosaic of the AEGIS field, alongside the overlapping *XMM-Newton* observations, we produced an X-ray catalogue.
Results. The analysis revealed the possible presence of structures with masses of $4 \times 10^{13}\ M_{\odot}$ at redshift 0.75, highlighting the depth of the survey. Comparing results with those from two other cluster catalogues provided by AMICO and VT, we found 43 common clusters with cluster centre offsets of 100 ± 60 kpc and redshift differences below 0.001. We provide a comparison of the cluster catalogues with a catalogue of massive galaxies and report on the significance of cluster selection. In general, we were able to recover approximately 75% of the galaxies with $M^{\star} > 2 \times 10^{11}\ M_{\odot}$.
Conclusions. This study emphasises the potential of the J-PAS survey and the employed techniques, including down to group scales.

Key words. methods: statistical – galaxies: clusters: general – galaxies: groups: general

1. Introduction

Galaxy clusters are powerful tracers of cosmic structure formation. Linked to massive overdensity peaks in the universe, cluster abundance as a function of mass and redshift provides a compelling tool to constrain cosmological parameters (e.g. Carlberg et al. 1996; Reiprich & Böhringer 2002; Voit 2005; Allen et al. 2011; Weinberg et al. 2013; Pacaud et al. 2016; Costanzi et al. 2019; Ider Chitham et al. 2020; Giocoli et al. 2021; Lesci et al. 2022a,b). Thus, the identification and characterisation of galaxy clusters in different wavelengths and numerical simulations allow us to refine our understanding of the universe's structure, evolution, and fundamental physics.

Wide-field cosmological surveys, such as the Dark Energy Survey (The Dark Energy Survey Collaboration 2005), KiDS (de Jong et al. 2013), J-PAS (Benitez et al. 2014), and in the near future, Euclid (Euclid Collaboration 2022) provide information about billions of galaxies. Of particular interest to group and galaxy cluster detection, sophisticated algorithms and data analysis techniques have been developed to identify and catalogue large-scale structures and characterise physical properties such as mass, morphology, stellar mass content, and gas properties. These algorithms employ diverse methodologies, including detecting overdensities in galaxy distributions, analysing multi-wavelength data, and utilising machine learning techniques. In this work, we focus on a specific cluster finder, the adaptive wavelet filtering technique PZWav (Gonzalez 2014; Werner et al. 2023), and we compare its results with those from the Voronoi tessellation (VT) method (Ramella et al. 2001; Lopes et al. 2004) and the Adaptive Matched Identifier of Clustered Objects (AMICO) algorithm (Bellagamba et al. 2019; Maturi et al. 2019). Cluster finders such as AMICO and PZWav have been developed with the ability to exploit the photometric information in the form of a redshift probability density function (PDF). This feature has been proven to be particularly valuable in the recent imaging surveys that utilise narrow-band filters (e.g. Benitez et al. 2014; Bonoli et al. 2021; Martí et al. 2014; Mendes de Oliveira et al. 2019; Cenarro et al. 2019), as it enables the harnessing of precise photometric redshift estimates of galaxies.

In this study, we utilise the accurate photometric redshift estimates obtained from the miniJPAS survey (see details in Sect. 2) to assess the strengths of the recently started wide J-PAS survey. Our analysis focuses on testing the performance of the PZWav cluster finder and its comparison to the other two methods (VT and AMICO), extending the limits to the regime of low-mass groups. As the miniJPAS data set also provides reliable spectral energy distribution (SED) estimates (González Delgado et al. 2021, 2022), we characterise the identified structures by evaluating richness, optical luminosity, and total stellar mass. The paper is organised as follows. In Sect. 2 we describe the photometric information obtained from the miniJPAS survey. Section 3 presents the details of the chosen algorithm to detect the galaxy cluster candidates and introduces

* PZWav and VT galaxy cluster catalogues are available at the CDS via anonymous ftp to cdsarc.cds.unistra.fr (130.79.128.5) or via https://cdsarc.cds.unistra.fr/viz-bin/cat/J/A+A/685/A98

the adaptive membership estimator utilised to characterise the cluster sample. In Sect. 4, we outline the galaxy cluster catalogue, propose two absolute magnitude regimes, and discuss a richness selection. In Sect. 5, we show the matching cluster candidates within the overlapping AEGIS[1] X-ray field, we provide scaling relations given the mass tracers, and we discuss the properties of catalogues obtained from different algorithms. We also present the significance of our results based on a catalogue of massive galaxies. We summarise and conclude in Sect. 6. Throughout this work, we adopt a flat ΛCDM cosmology with $H_0 = 68\,\mathrm{km\,s^{-1}\,Mpc^{-1}}$, $\Omega_\mathrm{m} = 0.31$, in agreement with Planck Collaboration XIII (2016) parameters. Magnitudes are given in the AB system.

2. Data

We utilised the photometric data obtained by Hernán-Caballero et al. (2021) from the miniJPAS survey (Bonoli et al. 2021), which comprises a set of 54 narrow-band (full width half maximum, $FWHM \sim 145$ Å, following the Sloan Digital Sky Survey broad-band filters u, g, r, i) along with two broadband filters extending to the near-infrared and the near-UV. This survey covers an approximate area of one square degree on the Extended Groth Strip field. The miniJPAS data set served as a pathfinder for the recently started wide-field cosmological survey named the Javalambre-Physics of the Accelerated Universe Astrophysical Survey (J-PAS). Conducted from the Javalambre Observatory in Spain, the survey employs a dedicated 2.5 m telescope and a 1.2 Gpix camera capable of capturing an area of 4.7 sq. deg of the sky in a single shot (Benitez et al. 2014). The complete survey aims to observe 8500 sq. deg using the filter system described above.

The z_phot were estimated using a customised version of the LePhare code (Arnouts & Ilbert 2011), which has been specifically optimised to replicate the J-PAS filter system. This code computes the z_phot PDF by weighting the log-likelihood distribution with a prior that accounts for the redshift distribution, considering the magnitude and colour of the galaxies. The prior function is derived from the galaxy spectroscopic redshift distribution obtained by the VIMOS VLT Deep Survey (Le Fèvre et al. 2005), which also provides the redshift and spectral type PDFs in the i-band magnitude.

To understand and characterise the z_phot performance, Hernán-Caballero et al. (2021) and Laur et al. (2022) analysed sub-samples of galaxies with available spectroscopic redshifts in the miniJPAS catalogue. The study performed by Hernán-Caballero et al. (2021) revealed a typical z_phot uncertainty of $\sigma_{\mathrm{MAD},z} = 0.013$ for galaxies with a magnitude in r-band $r < 23$. As a subsequent work, Laur et al. (2022) presented a new z_phot workflow to provide redshift estimates for the J-PAS survey.

In González Delgado et al. (2021, 2022), the authors present in detail the procedure to estimate the stellar mass of the galaxies from the J-spectra. The application of the SED fitting code `BaySeAGal` (González Delgado et al. 2021) allows the PDF of the stellar population properties to be retrieved, such as stellar mass, based on the galaxy's star formation rate, luminosity, and the mass loss due to stellar evolution.

This first data release from the miniJPAS provides an ideal data set for refining various strategies related to galaxy cluster detection and analysis. These investigations offer consistent insights for the J-PAS survey.

[1] All-Wavelength Extended Groth Strip International Survey.

3. Methods

This section provides details regarding the PZWav detection algorithm and the run parameters utilised in this analysis. Additionally, we introduce a probabilistic approach to characterise the cluster sample, focusing on identifying potential galaxy members within a characteristic radius.

3.1. PZWav algorithm

There is a myriad of algorithms for the detection of galaxy clusters using optical data (for a review Gal 2006; Euclid Collaboration 2019). Among them, PZWav (Gonzalez 2014; Werner et al. 2023) and AMICO (Bellagamba et al. 2019; Maturi et al. 2019) are particularly suitable for J-PAS due to their capacity to handle not only the nominal values of the photometric redshifts but also their PDFs. PZWav is a density-based algorithm that requires minimal assumptions about cluster properties, making it complementary to matched-filter approaches such as the one implemented in AMICO, for instance.

PZWav detects structures by identifying overdensities on fixed physical scales associated with clusters. It requires information such as the sky coordinates of galaxies, photometric redshifts, and magnitudes. The algorithm creates a series of redshift slices, with each galaxy assigned a weight based on the probability of its redshift lying at the respective bin. By integrating the probabilities over the redshift limits of each bin, the code generates 2D galaxy density maps. These maps are convoluted with a difference-of-Gaussians kernel, which enhances cluster-sized structures while diminishing the impact of smaller and larger structures. Additionally, to estimate the related noise, a separate set of density maps is created by randomising the projected positions of galaxies within the redshift slice[2].

In each redshift slice, a galaxy cluster candidate is identified as a peak in the density map that exceeds the noise threshold. The cluster centre is defined as the position of the local highest peak, and the final redshift of the cluster is determined by computing the median z_phot of the galaxies within a redshift range $\Delta z = 0.02$ (equivalent to twice the bin width) and a physical radius of $R = 500$ kpc. To identify the structures, we defined redshift slices with a width of $\mathrm{d}z_\mathrm{w} = 0.01$ and constrained the cluster smoothing kernel scales to 400 and 1400 kpc.

For the algorithm, a signal-to-noise ratio is defined as the amplitude of the highest peak in the density maps in relation to the noise level. The noise level is calculated as the standard deviation of a Gaussian approximation obtained from density maps produced by a randomised set of coordinates for the galaxy positions. For this analysis, the default detection threshold was set to $S/N_\mathrm{thr} = 4$. Tests with simulations, as described in Werner et al. (2023), indicate that our catalogue is expected to be 85% pure and 80% complete. As the simulations were tailored for S-PLUS data, with broader photo-z PDFs, these values should be taken as lower thresholds[3]. To prevent clusters passing through a collision event from being counted twice, we set as merging parameters $\mathrm{d}r_\mathrm{lim} = 1500$ kpc and $\mathrm{d}z_\mathrm{m} = 0.03$ as the minimum distance between two structures in both plane-of-sky and redshift spaces.

[2] This is slightly different than the approach used for MaDCoWS2 (Thongkham et al, in prep.) where the positions are preserved but the PDFs are shuffled.

[3] In Werner et al. (2023), the authors used a prior version of PZWav with slightly different key parameters used to optimise the performance for the S-PLUS survey (Mendes de Oliveira et al. 2019). Their method of noise calculation is similar to the method used in our work.

In our study, we consider all galaxies brighter than $m = 22.7$ in the r-band to ensure the completeness of the observations. No cuts or selection criteria were applied based on $z_{\rm phot}$ quality, colour, or other factors. This approach allowed us to analyse the full galaxy sample, providing a complete view of the cluster population.

3.2. An adaptive membership estimator

For further characterisation of the cluster detection catalogue, we used a probabilistic approach to estimate galaxy memberships. While spectroscopic surveys ideally provide accurate membership information, their demanding observational requirements make achieving high coverage fractions of cluster galaxies challenging. Therefore, the availability of photometric surveys encourages the development of strategies that rely on photometric information to estimate galaxy memberships.

The detection algorithm PZWav does not provide a galaxy member catalogue alongside the cluster candidate detection. Therefore, we developed an adaptive membership estimator (AME) that is density based and that we aimed to be as data based and assumptions-free as possible. This AME utilises the cluster information in the $(2 + 1)D$ space, specifically the cluster redshift ($z_{\rm cl}$), sky positions ($\rm RA_{cl}$ $\rm Dec_{cl}$), and the galaxies $z_{\rm phot}$ and PDFs (For a detailed review of the method and its application on a simulated data set, see Doubrawa et al. 2023).

In the following, we summarise the relevant steps of the algorithm. First, we excluded obvious non-members beyond a radius of 2.5 Mpc in the plane of sky from the cluster centre and with $|z_{\rm phot} - z_{\rm cl}| > 3\sigma_{{\rm MAD},z}(1 + z_{\rm cl})$, where $\sigma_{{\rm MAD},z}$ is the photo-z error, as presented in Sect. 2 ($\sigma_{{\rm MAD},z} = 0.013$, Hernán-Caballero et al. 2021). Then, we defined an aperture radius ($R_{\rm c}$) characterised by a change of a factor of approximately two in the radial density profile of galaxies, as found in Doubrawa et al. (2023) through simulations. This parameter highlights the change from cluster to field-dominated galaxies. We then shuffled the redshift of each galaxy within $R_{\rm c}$ by randomly assigning a value based on the galaxy photo-z PDFs ($z_{\rm PDF}$). We applied a 3σ clipping on the velocity dispersion estimated with $z_{\rm PDF}$ to avoid contamination by field galaxies. With the remaining galaxies, we applied HDBSCAN[4] (Campello et al. 2013), a density-based clustering algorithm that connects galaxies that are spatially close and that considers isolated galaxies as interlopers. This step identifies the largest group of galaxies linked by HDBSCAN as cluster members. To use the full photo-z PDF information, we repeated the last two steps 100 times. The final membership probability ($P_{\rm mem}$) for a given galaxy was then defined as the number of times it is selected as a member galaxy over the total number of iterations.

3.3. Cluster characterisation

One of the main attributes of J-PAS, and also miniJPAS, is its high precision achieved through the filter system. The characterisation and template fittings, incorporating colour and galaxy extinction information, result in accurate measurements of absolute magnitudes and stellar mass (González Delgado et al. 2021, 2022). Exploring these attributes, we characterised the cluster sample by estimating richness, total optical luminosity, and total stellar mass within $R_{\rm c}$. We present the results in two different absolute magnitude limits (−19.5 and −21.25), as presented in detail in Sect. 4.3.

[4] Hierarchical Density-Based Spatial Clustering of Applications with Noise.

Table 1. Galaxy cluster detection catalogue columns and description.

ID	PZWav cluster identification number
RA	PZWav position in the sky in RA
Dec	PZWav position in the sky in Dec
z	PZWav redshift
SNR	PZWav signal-to-noise
λ–19.5	Richness estimates ($M_r < -19.5$)
λ_err–19.5	Uncertainty in λ ($M_r < -19.5$)
Lum–195	Optical luminosity ($M_r < -19.5$) [$L_\odot$]
Lum_err–19.5	Uncertainty in L_λ ($M_r < -19.5$) [$L_\odot$]
Mstar–19.5	Stellar mass ($M_r < -19.5$) [$M_\odot$]
Mstar_err–19.5	Uncertainty in $M^\star_\lambda$ ($M_r < -19.5$) [$M_\odot$]
λ–21.25	Richness estimates ($M_r < -21.25$)
λ_err–21.25	Uncertainty in λ ($M_r < -21.25$)
Lum–21.25	Optical luminosity ($M_r < -21.25$) [$L_\odot$]
Lum_err–21.25	Uncertainty in L_λ ($M_r < -21.25$) [$L_\odot$]
Mstar–21.25	Stellar mass ($M_r < -21.25$) [$M_\odot$]
Mstar_err–21.25	Uncertainty in $M^\star_\lambda$ ($M_r < -21.25$) [$M_\odot$]

We defined richness as the sum of the probabilities of all galaxies associated with a given cluster, calculated as $\lambda = \sum_i P_{{\rm mem},i}$. Similarly, the total optical luminosity was determined by summing the luminosity of each galaxy, $L_i = 10^{0.4[4.65-R_i]}$, weighted by the galaxy pertinence, $L_\lambda = \sum L_i P_{{\rm mem},i}$. Here, 4.65 represents the solar absolute magnitude in the r-band (Willmer 2018), and R_i is the galaxy absolute magnitude in the same band. Additionally, we could derive the total stellar mass of the cluster sample by summing the stellar masses of individual galaxies ($M^\star_i$) weighted by their membership probabilities, resulting in $M^\star = \sum_i M^\star_i P_{{\rm mem},i}$.

4. PZWav's Galaxy cluster catalogue

In this section, we present the properties of the resulting galaxy cluster catalogue. We examine the impact of applying different absolute magnitude limits focusing on the completeness of the catalogue at high redshifts and a better characterisation of clusters at low redshifts. Furthermore, we discuss an implementation of a richness selection to improve the catalogue purity by removing possible detections by chance.

4.1. Catalogue

Running the PZWav algorithm on the miniJPAS area, we obtained a catalogue with 574 galaxy groups and cluster candidates in the redshift range of $0.05 < z < 0.8$ (in agreement to previous studies of Maturi et al. 2023, in the same area), above an S/N of four. The catalogue provides essential information, including the identification number, sky coordinates, photometric redshift, and detected S/N of each cluster. Additional properties, such as richness, total stellar mass, and optical luminosity are given for two different absolute magnitude ranges (as discussed in Sect. 4.3). Table 1 provides a summary of the available columns in the catalogue along with their corresponding descriptions.

In Fig. 1, we present the catalogue's redshift (top panel) and S/N distributions in histograms (bottom panel). We highlight two distinct samples: the complete catalogue, represented by the grey bars, which includes all clusters detected above the S/N threshold of four, and the refined sample (discussed in Sect. 4.4), indicated with blue bars.

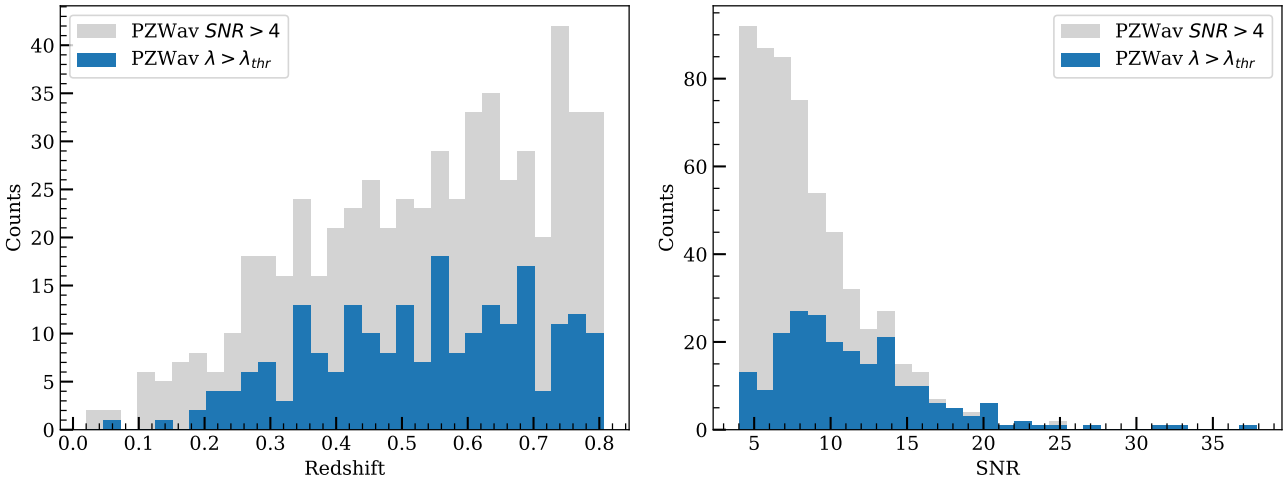

Fig. 1. Properties of the PZWav catalogue. Left panel: redshift distribution of the cluster candidates. Right panel: PZWav S/N distribution. Both histograms show the sample before (grey) and after (blue bars) the richness selection. We applied $\lambda_{\rm thr}$ of 1.9 and 3.0 for cluster and group regimes (as discussed in Sect. 4.3).

Table 2. Galaxy membership catalogue columns and description.

ID	Identification number
RA	Position in the sky in RA
Dec	Position in the sky in Dec
photo_z	Photometric redshift
MAG_AUTO	Apparent magnitude in r-band
ClusterID	Corresponding cluster ID
Pmem-19.5	Membership probability for $M_r < -19.5$
Pmem-21.25	Membership probability for $M_r < -21.25$

4.2. Cluster member catalogue

Understanding the membership composition of galaxy clusters is crucial for a comprehensive analysis of their properties and dynamics. In this section, we present the membership catalogue produced by AME (Sect. 3.2), a fundamental component of our study, that allowed us to identify and characterise the galaxies that belong to the detected galaxy clusters.

The catalogue comprises 9070 galaxy members, which account for 82% of the available galaxy catalogue provided by the mini-JPAS survey, after applying the selection magnitude ($m_r < 22.7$) and redshift cuts ($0.05 < z < 0.8$). Table 2 provides an overview of the key information included in the membership catalogue. This data set contains essential data, such as sky positions, photometric redshift, photo-z PDF, and membership probability. The membership probability, $P_{\rm mem}$, is listed for two absolute magnitude limits, which are further discussed in detail in Sect. 4.3.

A detailed analysis of the membership significance and statistics can be found in Doubrawa et al. (2023). In addition to the galaxy catalogue obtained by the PZWav algorithm, we extended our analysis to include membership catalogues for the diverse cluster catalogues investigated throughout this study. The catalogues can be found at the J-PAS website.

4.3. Group and cluster regimes

To avoid systematic errors in richness, total luminosity, and stellar mass estimations, such as the incompleteness of the galaxy catalogue due to the redshift range, we chose to work in two different regimes. In the "cluster regime", we considered galaxies with an absolute magnitude below $M_r < -21.25$, ensuring a volume-limited sample up to a redshift of $z = 0.8$. The "group regime", with an absolute magnitude limit of $M_r < -19.5$, is valid for $z < 0.3$, as proposed by Zheng & Shen (2021). Considering their different luminosity properties, these regimes allowed us to study structures with a different focus, with a brighter cut benefiting galaxy group-like structures.

In the left panel of Fig. 2, we present the richness estimates for the galaxy cluster candidates concentrated within the redshift range of $0.05 < z < 0.3$. We compare the richness estimates obtained with the two absolute magnitude cuts of $M_r < -21.25$ (cluster regime) and $M_r < -19.5$ (group regime). The blue points in the left panel show the median richness values, with error bars representing the dispersion of the sample. The figure highlights the larger values in richness estimation when considering fainter magnitudes. For instance, systems that are overlooked with a richness of $\lambda = 0$ using the bright magnitude cut increase to $\lambda = 4.2$ when fainter galaxies are included.

The right panel of the figure focuses on the S/N provided by PZWav for the selected candidates. It is important to note that we did not apply additional magnitude cuts while running the detection code, as some detection codes allow the constraint of the apparent magnitude to be $m_{\rm cut} = m_* + 1.5$. Therefore, when analysing the detected structures in the cluster regime, we observed that some of them exhibit a richness value of $\lambda = 0$ and still show a high S/N. This indicates that these candidates have a high-density amplitude compared to the background noise and were not adequately described by the selected bright absolute magnitude cut. However, when the group regime is applied, the richness values are correctly estimated, allowing for a more accurate characterisation. This test emphasises the importance of considering different magnitude ranges depending on the desired significance level.

4.4. Generating a refined catalogue using richness

One of the challenges in galaxy cluster detections is assessing the contamination and completeness of the resulting catalogue. The presence of false structures can introduce biases in the measurements of cluster abundances, thus affecting our understanding of the underlying cosmological parameters based,

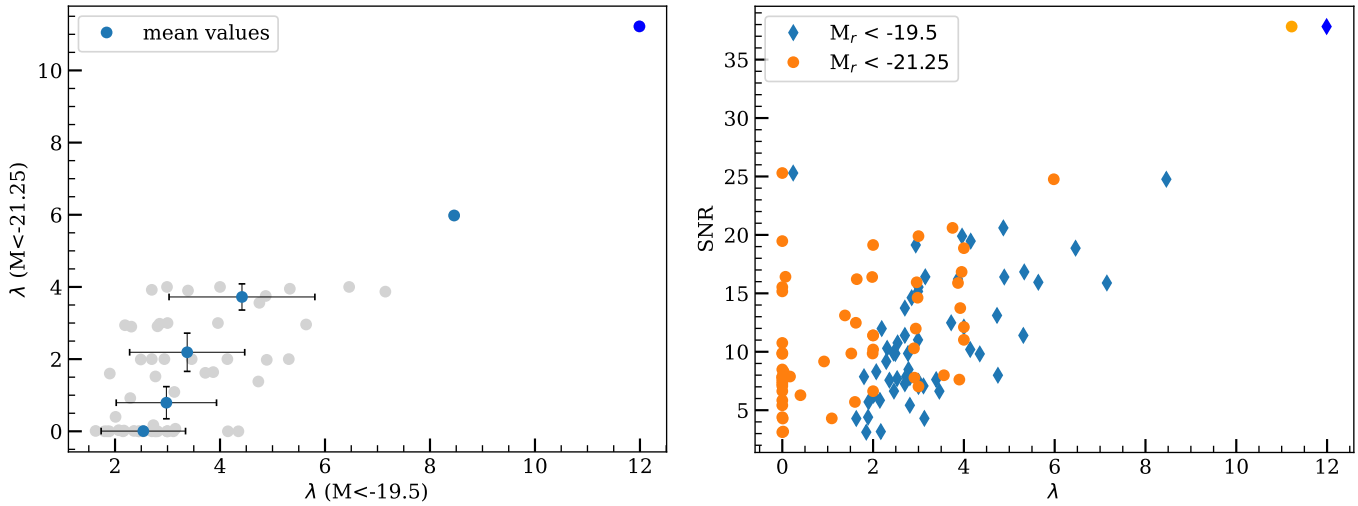

Fig. 2. Differences found in richness estimates. Left panel: comparison within richness calculated in two different absolute magnitude cuts: group regime ($M_r < -19.5$), for structures with $z < 0.3$, and cluster regime ($M_r < -21.25$), within $0.3 < z < 0.8$. Right panel: PZWav S/N in the function of the derived richness. Some groups overlooked in the cluster regime can have a significant richness in shallower magnitude cuts.

for example, on counts and clustering. Studies with simulated sky areas presented by Werner et al. (2023) for the S-PLUS survey (Mendes de Oliveira et al. 2019) have shown that PZWav $S/N > 3.3$ achieves the best values of completeness and purity. In contrast, other approaches, such as the one proposed by Rykoff et al. (2014), adopt a distinct selection method, using a richness threshold of 20 galaxies to limit their sample for higher mass clusters.

We propose an alternative approach to address contamination in the catalogue. Following a similar methodology described in Klein et al. (2017), we developed a selection criteria based on the richness that allows us to remove cluster candidates below a certain threshold. The method involves the comparison of the PZWav catalogue with randomly distributed points in both sky positions and redshifts. We expect to find small richness values, as these sky positions are not privileged, but sometimes, this distribution may reach a galaxy overdensity and provide a meaningful measurement. For each PZWav cluster candidate, we evaluated the number of random points within a specific redshift bin defined by $|z_{\mathrm{opt},i} - z_{\mathrm{rand}}| < 0.05$ (as $3\sigma_{\mathrm{MAD},z}$). We then calculated the fraction of these points with a richness value lower than the richness of the ith PZWav candidate. This process provides a quantitative measurement of the significance of the calculated richness compared to the randomly distributed points.

To minimise the possibility of misidentifying a galaxy group as contamination due to the magnitude cut (as presented in Sect. 4.3), we repeated the above analysis in the two magnitude regimes and obtained two different richness values. Therefore, by setting a significance threshold of 90%, we established richness limits of 1.9 and 3.0 for the cluster and group regimes. As a result, the final content of the catalogue is reduced to only 38% of the initial cluster candidate sample. The impact of this cut-off is evident in the altered distributions of redshift and S/N, as illustrated by the blue bars in Fig. 1.

As this procedure aims to attain a purer sample, it inevitably results in a loss of completeness. To comprehensively understand the impact of these trade-offs on our results, a simulated catalogue replicating the miniJPAS area would be essential. Unfortunately, such a catalogue is currently unavailable.

In Fig. 3 we present the richness distribution as a function of redshift for both the group (blue) and cluster regimes (orange).

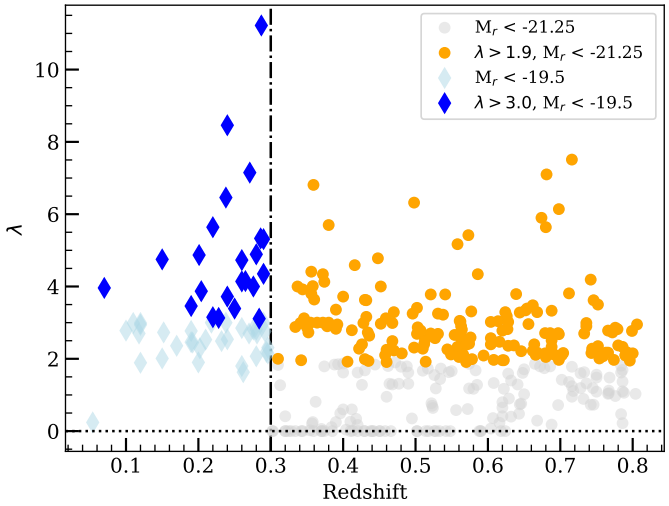

Fig. 3. Richness distribution of the cluster candidates detected by PZWav for both group (blue) and cluster regimes (orange) – before (lighter) and after (darker colours) the richness threshold. The dashed line indicates the redshift transition at $z = 0.3$, and the dotted one as the $\lambda = 0$.

The lighter colours represent the distribution before applying the richness threshold, while the darker colours symbolise the distribution after the threshold is applied. Within the identified structures, there is a specific cluster, mJPC2470−1771, that exhibits a high richness value of 11.5 ($M_r < -19.5$) at redshift $z = 0.29$, and it has been studied by Rodríguez-Martín et al. (2022).

Finally, following the richness selection criteria, we obtained a refined catalogue. The optical properties range from $1.9 < \lambda < 12$ for the richness, $10.6 < \log_{10}(L_\lambda/L_\odot) < 11.8$ for optical luminosity, and $10.6 < \log_{10}(M^\star_\lambda/M_\odot) < 12.2$ for stellar masses.

5. Results

In this section, we explore and compare the PZWav galaxy cluster catalogue with others previously presented in the literature. We focus on identifying the optical counterparts within the overlapped region of the AEGIS X-ray survey (Erfanianfar et al. 2013) and create a new X-ray catalogue based on PZWav centre

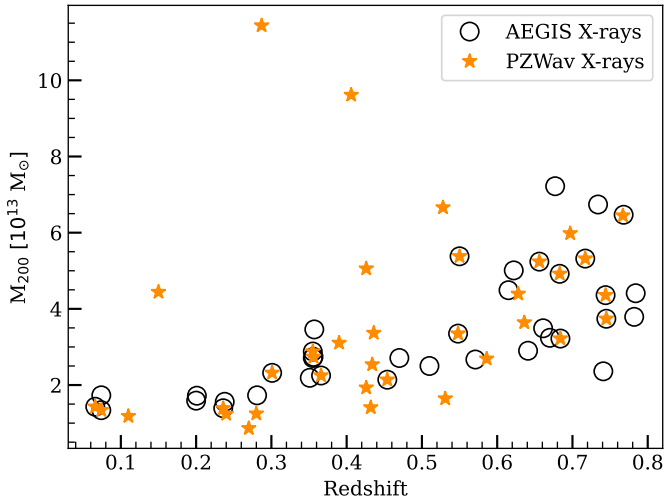

Fig. 4. Mass and redshift distributions of the PZWav optical detections that present an X-ray counterpart (orange stars). The black open circles show Erfaniafar's detection catalogue for the overlapping area. We have 17 clusters with a matching centre distance below 500 kpc and a redshift offset of $\Delta z < 0.05$. Masses are inferred from the weak lensing calibration of Leauthaud et al. (2010).

estimations. With the available masses, we derive scaling relations with the optical proxies provided by AME. Furthermore, we compare different optical catalogues produced for the miniJPAS by VT and AMICO algorithms, which are discussed in more detail in Sects. 5.4.1 and 5.4.2. We investigate the variations in centralisation and redshift estimations by highlighting the galaxy clusters that exhibit clusters that are identified by the three cluster finders simultaneously. Additionally, we present statistical analyses of the optical proxies for both matched and non-matched structures across these catalogues. Finally, we evaluate the significance of each optical catalogue by utilising the galaxy data as a reliable estimator.

5.1. Comparisons to AEGIS X-ray catalogue

The miniJPAS survey and the AEGIS survey (Davis et al. 2007) have an overlapping area, allowing for a comparison between optical and X-ray catalogues. The X-ray catalogue, created by Erfanianfar et al. (2013) using data from the *Chandra* and *XMM-Newton* telescopes, consists of 52 clusters within the redshift range of $0.06 < z < 1.54$. These clusters and groups present a mass range of $M_{200} \sim 1.34 \times 10^{13}$–$1.33 \times 10^{14}\, M_\odot$. We constrained the catalogue in order to focus our analysis on the specific area of miniJPAS and the desired redshift range ($0.05 < z < 0.8$), resulting in a selection of 36 clusters.

To establish a correspondence between the PZWav optical and X-ray catalogues, we performed a matching process based on the closest distances between centres and redshift offset. We applied a maximum centre difference of 0.5 Mpc and in redshift $\Delta z = 0.05$ (as $3\sigma_{\mathrm{MAD},z}$).

This matching procedure resulted in 17 counterparts. From these, seven detections were located at low redshift ($z < 0.55$), while 10 were found within the higher redshift range of $0.55 < z < 0.8$. We set the transition point at 0.55, aligning with the threshold used in Maturi et al. (2023). In Fig. 4, we present the mass distribution as a function of redshift for the X-ray groups represented as open circles.

Once we had identified the matching counterparts, we could then calculate the differences in centralisation and redshift for the matching sub-sample. These differences hold significant value, particularly in gravitational lensing analyses, as they can introduce biases that impact the final results (Parroni et al. 2017; Sommer et al. 2022). However, accurately modelling miscentering offsets without a large sample can be challenging. Therefore, this study focuses on observing potential trends rather than providing a comprehensive analysis of miscentering effects.

In general, the median variations found in centre positions between the catalogues are 125 ± 60 kpc. Regarding redshifts, 90% of the matched detections have offsets within 0.02 for both low and high redshifts. The median values are similar within the comparisons, 0.001 ± 0.005, for the entire redshift range. These findings suggest that the chosen matching criteria are appropriate, and increasing the thresholds would not significantly improve the number of successful matches.

5.2. Extended X-ray catalogue

To enhance the comparison, we reanalysed the same *Chandra* mosaic of the AEGIS field, implementing a lower detection threshold of 3σ (compared to 4σ in Erfanianfar et al. 2013). This new analysis takes advantage of *Chandra* PSF, which removes contaminating point sources to an order of magnitude lower flux. In addition, we added to the mosaic the *XMM-Newton* observations that overlap with the miniJPAS field. This not only contributed to improved large-scale background subtraction but also proved to be valuable for identifying newly discovered sources. Given our focus on the cross-matched sample, we established a systematic procedure for X-ray source identification, ensuring the consistency and replicability of our analyses.

We performed a positional match between the PZWav optical and X-ray sources, allowing a maximum offset of 0.5 Mpc. Some X-ray sources had more than one optical counterpart. In cases where an X-ray source had multiple counterparts, we employed a richness threshold-based approach to assess the significance of the matches, as discussed below. Optical groups that were determined to be chance associations with X-ray sources were removed from further analysis.

If an X-ray source still had multiple identifications after this step, it was excluded from the analysis of scaling relations unless one counterpart exhibited a richness that was significantly larger (by a factor exceeding 1.5). This criterion ensured that contamination from another group to the X-ray flux was limited to less than 30%, which is lower than the typical statistical error associated with the newly added sources.

For the catalogue of uniquely identified X-ray sources, we computed the rest-frame X-ray luminosity following the same procedures as outlined in Erfanianfar et al. (2013). We considered the aperture-to-total flux correction, the k-correction, and the total mass inferred by the weak lensing calibration of Leauthaud et al. (2010).

The steps resulted in a catalogue of 37 X-ray counterparts, including 20 detections within the redshift range of $0.05 < z < 0.55$ and 17 detections within the $0.55 < z < 0.8$ range. From those, 20 are new detections. We report the properties of the X-ray counterparts used in this analysis in Table A.1.

In Fig. 4, alongside the X-ray groups identified in Erfaniafar's catalogue (represented by open circles), we show the matched counterparts from the reanalysed sample with the PZWav optical catalogue (indicated by orange stars). The open circles with a central star symbol correspond to the 17 matches in Erfaniafar's catalogue. The most massive system, located at a redshift of $z = 0.29$ and exhibiting the highest richness, has a mass of $M_{200} = (1.14 \pm 0.07) \times 10^{14}\, M_\odot$. Previous mass estimates

Table 3. Linear regression fitting values.

Proxy	α	β	ϵ	$\bar{O}$
λ	13.47 ± 0.04	0.24 ± 0.51	0.039 ± 0.016	2.9
L_λ	13.48 ± 0.05	0.34 ± 0.18	0.076 ± 0.019	1.47
$M^\star_\lambda$	13.48 ± 0.05	0.23 ± 0.18	0.080 ± 0.021	3

Notes. The mass-observable model is described by Eq. (1), and L_λ and $M^\star_\lambda$ are given in units of $10^{11}\,L_\odot$ and $10^{11}\,M_\odot$.

based on X-rays alone presented by Bonoli et al. (2021) resulted in $M_{200} = (3.26 \pm 1.4) \times 10^{14}\,M_\odot$, a slightly larger value but with large uncertainty (~50%). While using Gemini GMOS spectroscopy follow-up, the same authors found $M_{200} = (2.2 \pm 0.3) \times 10^{14}\,M_\odot$.

We found a second interesting candidate located at $z = 0.41$, close to the survey borders, with an estimated mass of $9.6 \times 10^{13}\,M_\odot$. This object was already reported by Hsieh et al. (2005) as part of the Red-Sequence Cluster Survey (Gladders & Yee 2005) with a similar photometric redshift and within 10 arcsec. As far as we know, there is no dedicated discussion of this object in the literature, and it is a strong candidate for further study.

The lowest mass systems range from (0.72 ± 0.31) to $(1.60 \pm 0.24) \times 10^{13}\,M_\odot$ within the redshift range of $0.07 < z < 0.43$. Additionally, at redshift $z = 0.745$, we detected a system with a mass of $M_{200} = (3.75 \pm 0.5) \times 10^{13}\,M_\odot$ (also reported by Hsieh et al. 2005, at similar redshift and within 10 arcsec).

We stress that the successful detection of low-mass groups in our analysis highlights the depth of the miniJPAS survey. Moreover, it also demonstrates the effectiveness of our methodology, as also confirmed by the analysis of Maturi et al. (2023).

5.3. Scaling relations

Using LINMIX, a linear regression procedure with a Bayesian approach (Kelly 2007), we were able to perform the minimisation process considering the errors in both the X-ray mass estimates and the mass proxies. The relation was modelled as,

$$\log_{10}\left(\frac{M_{200c}}{M_\odot}\right) = \alpha + \beta \log_{10}\left(\frac{O}{\bar{O}}\right) + \epsilon, \quad (1)$$

where α and β are the coefficients, O is the mass proxy, $\bar{O}$ is the pivot value, and ϵ is the intrinsic random scatter about the regression. The best-fitting parameters are given in Table 3, and results are summarised in Fig. 5. With our sample, we could not find a strong correlation between the quantities. When comparing the mass proxies, we observed that the richness exhibits the highest scatter for the slope. This behaviour is further accentuated by the limited range of richness values in the sample, as well as the presence of two massive systems with a low richness that stands out from the overall distribution. In contrast, the optical luminosity shows a relatively steep slope, although still within the error bars.

We stress that our sample size is relatively small, which limits the robustness of our statistical results. However, with the ongoing J-PAS survey, we anticipate a larger sample size that will provide more reliable scaling relations.

Improving the scaling relations poses challenges, particularly in terms of mass estimation. The deep X-ray data available for miniJPAS allowed us to derive masses at the lower end of the spectrum, reaching a flux limit of $10^{-15}\,\mathrm{erg\,s^{-1}\,cm^{-2}}$. In comparison, other surveys such as the ROSAT all-sky survey and eROSITA (Merloni et al. 2012) have flux limits of $10^{-13}/10^{-12}$ and $10^{-14}\,\mathrm{erg\,s^{-1}\,cm^{-2}}$, respectively.

To address this limitation, Maturi et al. (2023) proposed alternative approaches. These include reanalysing the *XMM-Newton* archival data over the J-PAS footprint or

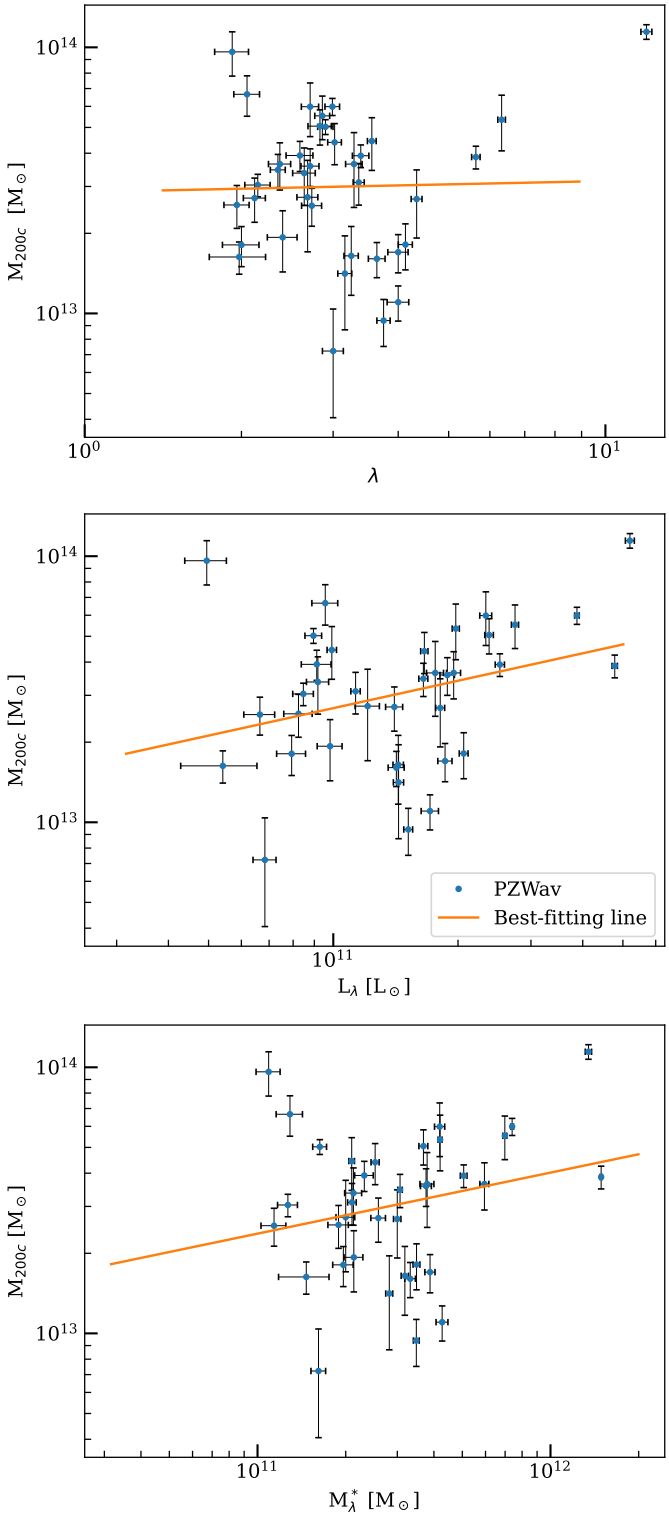

Fig. 5. Results obtained with the linear regression. Top panel: M_{200c} estimated from the X-ray luminosity and richness. Middle panel: M_{200c} versus optical luminosity, L_λ. Bottom panel: M_{200c} versus stellar mass, $M^\star_\lambda$. The orange lines represent the best-fitting values. Parameters can be found in Table 3.

incorporating weak gravitational lensing and velocity dispersion measurements into the analysis. These methods offer potential workarounds to improve mass estimation in the presence of flux limitations.

The mass estimates might also be affected by the dynamical state of the structure. Therefore, filtering the sample so that it comprises only the most relaxed (virialized) clusters could improve the scaling relations.

5.4. Comparisons between optical catalogues

Several computational algorithms can be employed to identify galaxy clusters in optical data, each with its own unique characteristics and capabilities. In the following sections, we provide a brief overview of two additional methods, namely, VT and AMICO. We present comparative results using the same miniJPAS data set, aiming to understand the differences among the samples detected by all methods or only by a specific method. To assess these variations, we utilised the AME estimator, which allowed us to quantitatively analyse the discrepancies between the different catalogues. We emphasise that this study is not intended to highlight the most correct catalogue (pure and/or complete) but rather to provide insights into different properties of the cluster sample, providing an improved analysis. We stress that there is a dedicated paper from Maturi et al. (2023) on the AMICO catalogue applied in the miniJPAS area.

5.4.1. VT

Considering a homogeneous distribution of particles, it is possible to define a characteristic volume associated with each particle. This is known as the Voronoi volume, whose radius is of the order of the mean particle separation. Voronoi tessellation has been applied to a variety of astronomical problems. A few examples can be found in Ikeuchi & Turner (1991), Zaninetti (1995), El-Ad et al. (1996), and Doroshkevich et al. (1997). Ebeling & Wiedenmann (1993) used VT to identify X-ray sources as overdensities in X-ray photon counts. Ramella et al. (2001), Kim et al. (2002), Lopes et al. (2004), and Soares-Santos et al. (2011) looked for galaxy clusters using VT. As pointed out by Ramella et al. (2001), one of the main advantages of employing VT to look for galaxy clusters is that this technique does not distribute the data in bins, nor does it assume a particular source geometry intrinsic to the detection process. The algorithm is thus sensitive to irregular and elongated structures.

The parameter of interest in our case was the galaxy density. When applying VT to a galaxy catalogue, each galaxy is considered a seed and has a Voronoi cell associated with it. The area of this cell is interpreted as the effective area a galaxy occupies in the plane. The inverse of this area gives the local density at that point. Galaxy clusters are identified by high-density regions composed of small adjacent cells, that is, cells small enough to give a density value higher than the chosen density threshold.

To detect galaxy clusters using VT, we used the code employed by Ramella et al. (2001). It uses the triangle C code by Shewchuk (1996) to generate the tessellation. The algorithm identifies cluster candidates based on two primary criteria. The first is the density threshold, which is used to identify fluctuations as significant overdensities over the background distribution, and it is referred to as the search confidence level (SCL). The second criterion rejects candidates from the preliminary list using statistics of VT for a Poissonian distribution of particles (Kiang 1966) by computing the probability that an overdensity is a random fluctuation. This is called the rejection confidence level (RCL). More details can be found in Ramella et al. (2001).

The main drawback of galaxy cluster selection from photometric data is contamination from background and foreground galaxies. A variety of approaches can be applied to deal with this problem. For instance, Kim et al. (2002) used a colour-magnitude relation to divide the galaxy catalogue into separate redshift bins and ran the VT code on each bin. The candidates identified in different bins were cross-correlated to filter out significant overlaps and produce the final catalogue. Ramella et al. (2001) and Lopes et al. (2004) followed a different approach, as they did not have colour information. Instead, they used the object magnitudes to minimise background and/or foreground contamination and enhance the cluster contrast. The galaxy data was split into overlapping magnitude bins, and the VT code was applied to each magnitude slice. The catalogues of cluster candidates from different layers were combined with a percolation analysis to produce a final list of candidates (see Ramella et al. 2001; Lopes et al. 2004 for further details).

Taking advantage of the great photometric redshift precision from J-PAS (0.3%), we could divide the input galaxy catalogue into separate photometric redshift slices and run the VT code on each slice. This approach represents a great improvement compared to cluster searches on regular photometric surveys, as it allows a more efficient minimisation of the background.

We ran the VT code on redshift slices of 0.04 and 0.05 from $z = 0.01$ to 0.8. The candidates identified in the different slices were cross-correlated to filter out significant overlaps and produce the final catalogue. These steps produced a catalogue with 159 cluster and group candidates.

5.4.2. AMICO

The AMICO algorithm (Maturi et al. 2019) is a cluster finder based on the search for cluster candidates with a redshift-dependent filter system that seeks to amplify the contrast between the cluster and noise models. It uses the r-band for detection as the default magnitude but also accepts one and/or combinations of other magnitudes.

The catalogue generated by AMICO with miniJPAS data contains 94 galaxy clusters for a signal-to-noise ratio larger than 2.5. It was performed through a redshift range of $0.05 < z < 0.8$. More details about the code, such as the run parameters, the probabilistic membership association, and the effects of the narrow-band photometry on galaxy cluster detection can be found in Maturi et al. (2023). In their study, the authors derived scaling relations for mass proxies, including amplitude A and estimates of the stellar mass. With a catalogue of cluster members identified through probabilistic associations, the authors showed a good agreement with spectroscopic memberships for galaxies with $P > 0.2$ and identified the brightest group galaxies (BGGs). Using AMICO and J-PAS, the study characterised galaxy groups and clusters, including down to small groups ($\sim 10^{13}\, M_{\odot}\, h^{-1}$).

5.4.3. Matching the catalogues

To compare the PZWav optical catalogue with the catalogues produced by AMICO and VT, we kept the same matching parameters used in the X-ray comparison, a maximum difference of 0.5 Mpc between the cluster centres and a redshift difference of $\Delta z = 0.05$. Through this procedure, we identified a total

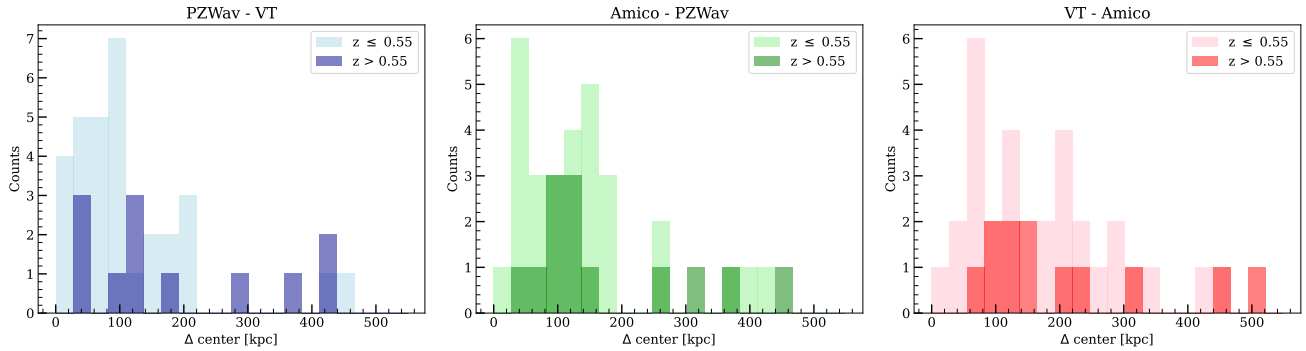

Fig. 6. Difference between centre coordinates of matching clusters identified by the three optical catalogues in a two-by-two comparison. The light colours represent clusters with redshifts lower than $z \leq 0.55$; dark colours are for $z > 0.55$. From left to right, blue is PZWav-VT, green is AMICO-PZWav, and red is VT-AMICO.

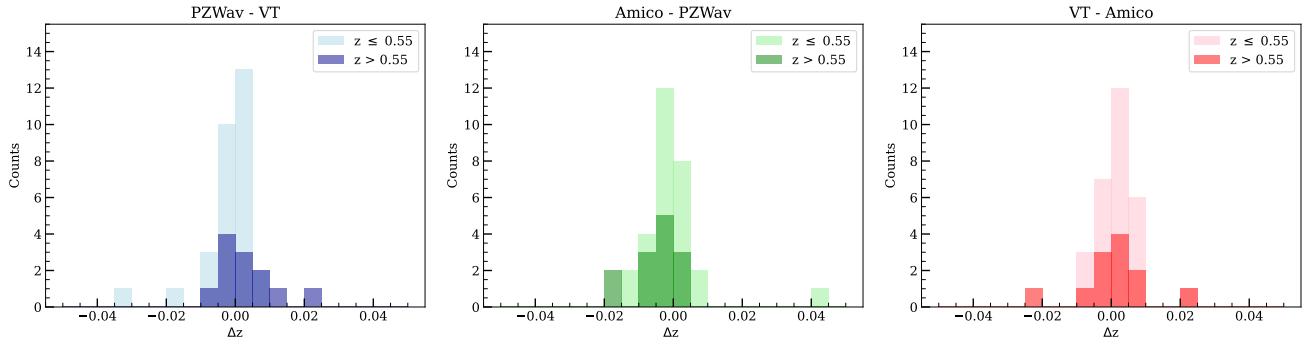

Fig. 7. Same as Fig. 6 but for the difference between redshifts of the detected structures.

of 43 clusters that are common to the three cluster finder catalogues. Figures 6 and 7 provide a visual comparison of these matched clusters, showing the agreement between the centre coordinates and redshifts in two-by-two combinations. In these figures, the blue bars represent the PZWav-VT comparison, the green bars indicate the AMICO-PZWav comparison, and the red bars show the VT-AMICO comparison. Figure 6 demonstrates that the cluster centres are well characterised, with more than 80% (35/43 structures) of the clusters having centre differences lower than 300 kpc. These offsets are lower for low-redshift clusters, with a median value of 92 ± 53 kpc for the PZWav-VT case (31), compared to the median value of 112 ± 67 kpc for the high-redshift clusters (12).

Figure 7 shows the results in terms of redshift offsets. Here, we observed that more than 90% (40/43) of the detections show a variation lower than ±0.02, 94% (29/31) for low-redshift clusters, and 91% (11/12) for high-redshift clusters. The median values of these redshift offsets are similar within the comparisons between the cluster finders, with an overall value of 0.001 ± 0.005 for the entire redshift range. Additionally, both the centre offsets and redshift differences exhibit exponential behaviour, indicating that the chosen matching parameters are appropriate.

In Fig. 8, we examined the distribution of the S/N of PZWav as a function of the richness (defined as the sum of the galaxies' membership probabilities) in the cluster regime. The distribution in the figure reveals a correlation between the quantities. When we applied the richness cut mainly removing structures with low S/N, we observed a decrease in density points for lower S/N values. This behaviour is also evident in the modified shape of the histogram shown in Fig. 1.

We also observed that most matches have an S/N greater than six. The common matches among the catalogues are denoted

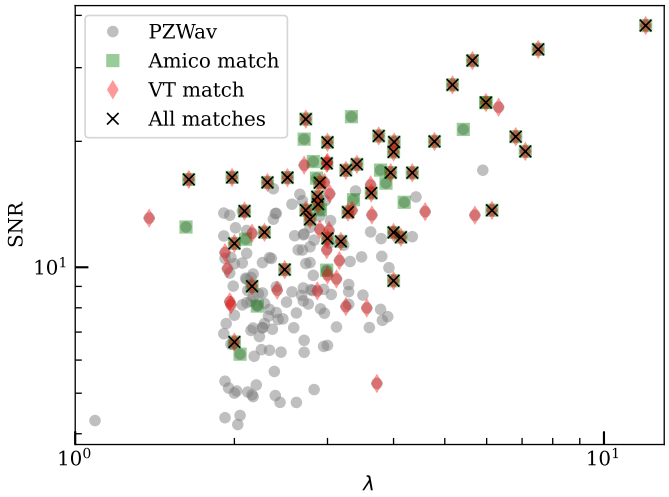

Fig. 8. Richness distribution in function of the S/N for the optical catalogues. PZWav is shown with grey dots, PZWav matches to VT are in red, and PZWav matches to the AMICO catalogue are in green. The matches between the three catalogues are indicated with x's. The apparent wall at $\lambda = 1.9$ is produced by the richness cut described in Sect. 4.4. Lower λ values are from structures with $z < 0.3$, which are affected by another richness threshold.

with x's, while the green squares and red diamonds represent the two-by-two matches between PZWav and AMICO, and VT, respectively. This analysis shows PZWav's sensitivity to the small density peaks.

By applying AME to the catalogues, we could provide additional characterisation of the detections using the mass proxies

Table 4. Median values of the optical proxies for each cluster catalogue divided between matched and non-matched clusters for richness, optical luminosity, and stellar mass.

	N° cl.	λ	L_λ	$M^\star_\lambda$
PZWav	43	3.18 ± 0.06	1.65 ± 0.07	3.49 ± 0.14
	178	2.58 ± 0.03	1.18 ± 0.02	2.13 ± 0.07
VT	43	3.22 ± 0.07	1.62 ± 0.07	3.24 ± 0.18
	116	1.73 ± 0.12	0.64 ± 0.06	1.12 ± 0.10
AMICO	43	3.00 ± 0.14	1.72 ± 0.10	3.64 ± 0.22
	51	1.87 ± 0.16	0.65 ± 0.09	1.22 ± 0.17

Notes. The term M_λ is given in units of $10^{11}\,M_\odot$ and L_λ in $10^{11}\,L_\odot$.

and compare the results with the sample identified by only one of the cluster finders (Sect. 5.4.4). In the following, we focused on the richness results to calculate the fraction of matched clusters to the total number of detections.

For PZWav, 85% of the catalogue exhibits similarity with the others for clusters with a richness (λ) greater than six. This percentage decreases to 30% for a richness within the range of $3 < \lambda < 6$ and to only 13% for λ less than three. We observed similar trends for VT and AMICO, with 75%, 57%, and 15% for VT and 100%, 62%, and 34% for AMICO in the same richness ranges. These values highlight the agreement between the catalogues. We discuss the significance of the catalogues further in Sect. 5.5.

5.4.4. Statistics on the mass proxies

In this subsection, we examine the differences between the properties of matched and non-matched galaxy clusters detected by different cluster finders. Table 4 displays the median values and deviations of richness, optical luminosity, and stellar mass for both the matched and non-matched clusters in the cluster regime.

For the clusters in the matched sample, we observed that the median values show similarities among the different cluster finders, with minor variations within the error bars. This can be attributed to the fact that the matched clusters have similar centre and redshift positions, as they are defined based on small offsets in these parameters. It is important to note that offsets can impact the detection of cluster members. A detailed discussion on how offsets can impact AME membership detection can be found in Doubrawa et al. (2023). Here, we highlight the values found for PZWav: $\lambda = 3.18 \pm 0.06$, $L_\lambda = (1.65 \pm 0.07) \times 10^{11}\,L_\odot$, and $M^\star_\lambda = (3.49 \pm 0.14) \times 10^{11}\,M_\odot$.

However, significant differences arose when analysing the non-matched sample. For example, in the case of PZWav, the richness of the non-matched clusters (178) is considerably lower, with a median value of 2.58 ± 0.03. This difference is even more pronounced for the VT and AMICO catalogues, where the relative difference exceeds 45%. As the PZWav catalogue is limited to $\lambda > 1.9$, the overall offsets are smaller. Similar trends can be observed for the other mass proxies.

We present the median values for the entire redshift range to ensure clarity. However, when examining the sample separately for high ($z > 0.55$) and low ($z < 0.55$) redshifts, the offsets become more significant, with a 75% difference for L_λ and an 85% difference for $M^\star_\lambda$.

Despite the challenge of distinguishing true detections in observations, this analysis emphasises the median properties of galaxy cluster candidates identified by the cluster finders, and these detections are therefore likely to be true clusters[5]. We note that the median values of richness for the non-matched detections in VT and AMICO are similar to the richness cut applied during the richness selection of the PZWav catalogue. By redoing the richness analysis, one can suggest that the discussed thresholds in Sect. 4.4 can be utilised to remove part of the contamination.

It is important to note that the non-matched structures having significantly smaller λ values does not indicate a limitation of the detection codes. Instead, it highlights the possible detection of smaller groups and clusters.

5.5. Significance of the detection catalogues

Galaxy clusters are also widely explored in the literature in order to study cluster galaxy evolution, as several processes act on the cluster components through the halo evolution (Evrard 1997; Ettori et al. 2009; Allen et al. 2011; Dvorkin & Rephaeli 2015). Thus, understanding the relation between the luminous properties of the galaxies and the dark matter halos (M_h), or stellar-to-halo mass relation (SHM), can provide clues about the role of different physical mechanisms that affect the environment. One can quantify the contribution of the brightest cluster and/or group galaxies (BCGs/BGGs) by constraining a focused SHM relation. For example, studies by Leauthaud et al. (2012a,b), and Gozaliasl et al. (2018) provide methods to estimate the halo mass associated with a given BCG based on its stellar mass.

With this relation in mind, we followed the curve derived by Gozaliasl et al. (2018), and we found that galaxies with stellar masses $M^\star > 2 \times 10^{11}\,M_\odot$ are expected to reside in halos with masses of 1.4×10^{13} to $1.4 \times 10^{14}\,M_\odot$. As the SHM relation presents a significant intrinsic scatter ($\sigma_{\log M^\star} \sim 0.25$, see Gozaliasl et al. 2018, for details), the applied limit cannot be taken to exclude the presence of less massive galaxies in halos but serves as a tool to probe the expected cluster halo masses in our survey. Although the true distribution of clusters in the survey area is unknown, we can compare the significance of our catalogues with the distribution of galaxies themselves.

To assess the association between galaxies and our cluster and/or group catalogues, we performed a matching procedure by selecting all galaxies within 1 Mpc of the optically selected cluster centre and within a redshift range of $\Delta z < 0.05$. Once identified and removed, we could estimate the fraction of galaxies without any association with the catalogues.

Figure 9 presents some conclusions for low ($0.2 < z < 0.3$) and high redshifts ($0.3 < z < 0.6$). We note that we do not have results for $z < 0.2$, as the catalogue does not present such high-mass galaxies at low redshifts. This behaviour can be attributed to the limited survey volume and the corresponding low probability provided by the galaxy stellar mass function (Li & White 2009). As PZWav is the largest catalogue, it also has the best matching rates for stellar mass lower than $4 \times 10^{11}\,M_\odot$ at high redshifts. In general, we were able to recover approximately 75% of the galaxies. This value increased to 83% for the low-redshift range, indicating that only 17% of the galaxies are isolated. Within 3 and $5.5 \times 10^{11}\,M_\odot$, all galaxies have an associated optical system.

Considering the first two bins from Fig. 9, within $2 < M^\star\,[10^{11}\,M_\odot] < 3$ (corresponding to halo masses between 1.4 and $4.1 \times 10^{13}\,M_\odot$) and $3 < M^\star\,[10^{11}\,M_\odot] < 4.2$ (0.41 to $1.4 \times 10^{14}\,M_\odot$), we analysed the fraction of galaxies associated with optical catalogues as a function of redshift. Figure 10 highlights

[5] To ensure this conclusion, one must rely on simulations.

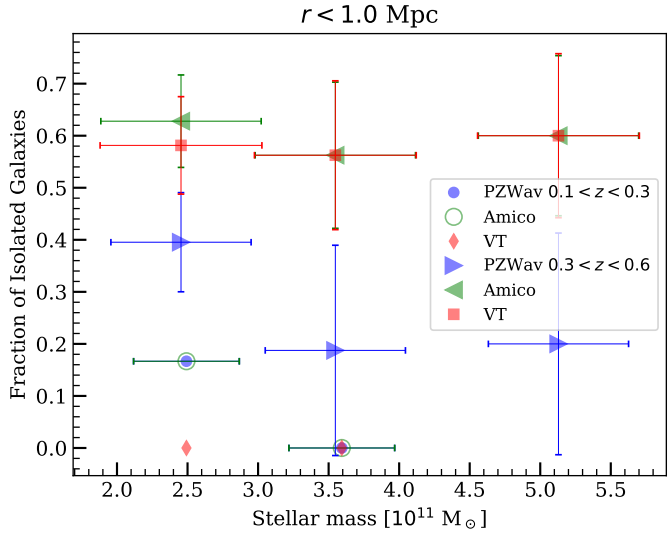

Fig. 9. Optical cluster finders PZWav, AMICO, and VT matched to the generated halo catalogue. The resulting curves give the fraction of galaxies of a given halo mass without any cluster association.

the results. The black lines represent the fraction of galaxies that have matches in the three optical catalogues, indicating a more reliable identification, with approximately 20% of galaxies being associated with clusters for $z > 0.3$.

In the first mass range of Fig. 10, VT (red) and AMICO (green) exhibit similar trends, providing good coverage up to $z = 0.3$. The cluster finder PZWav (blue) performs better at higher redshifts ($z > 0.5$). The pink curve in the figure represents the combined contribution of all the optical catalogues, demonstrating the improvement in the overall fraction rate. Additionally, the PZWav output with $S/N > 4$ is also shown as a grey curve, an experiment of the most complete scenario. In this case, only 20% of galaxies do not have an optical correspondence.

For the higher stellar mass range, $3 < M^{\star}\,[10^{11}\,M_{\odot}] < 4.2$, VT and AMICO exhibit similar behaviour up to $z = 0.6$, after which their contributions spread and change positions for $z > 0.7$. Due to its larger sample, PZWav shows better fractions across the entire redshift range, with a maximum value of 40% of isolated galaxies for $z > 0.65$.

As an additional analysis, the significance can be assessed in terms of the halo mass ($M_{\rm h}$) by following the relation derived between stellar and halo mass presented by Gozaliasl et al. (2018). For this, we followed a similar methodology as described above for estimating fractions of isolated galaxies within specific redshift bins while exploring various stellar mass thresholds. Our approach involved adopting redshift bins of width 0.2 with 0.1 overlaps and identifying the optimal stellar mass threshold that results in a maximum fraction of isolated galaxies of 0.2. With the minimum stellar mass results, we derived $M_{\rm h}$.

In Fig. 11, we illustrate $M_{\rm h}$ as a function of the mean redshift value within each bin for the three cluster finders. The PZWav cluster finder $\lambda > \lambda_{\rm thr}$ is represented by blue triangles, VT by red diamonds, and AMICO by green circles. To enhance visualisation, redshifts have been artificially displaced by 0.01 and 0.02 for VT and AMICO, respectively. The plot shows a similar trend among the cluster finders up to $z = 0.4$, but PZWav exhibits a higher coverage for $z > 0.55$ due to the larger number of detections. These results highlight the varying capabilities of different optical catalogues in detecting and associating galaxies with clusters.

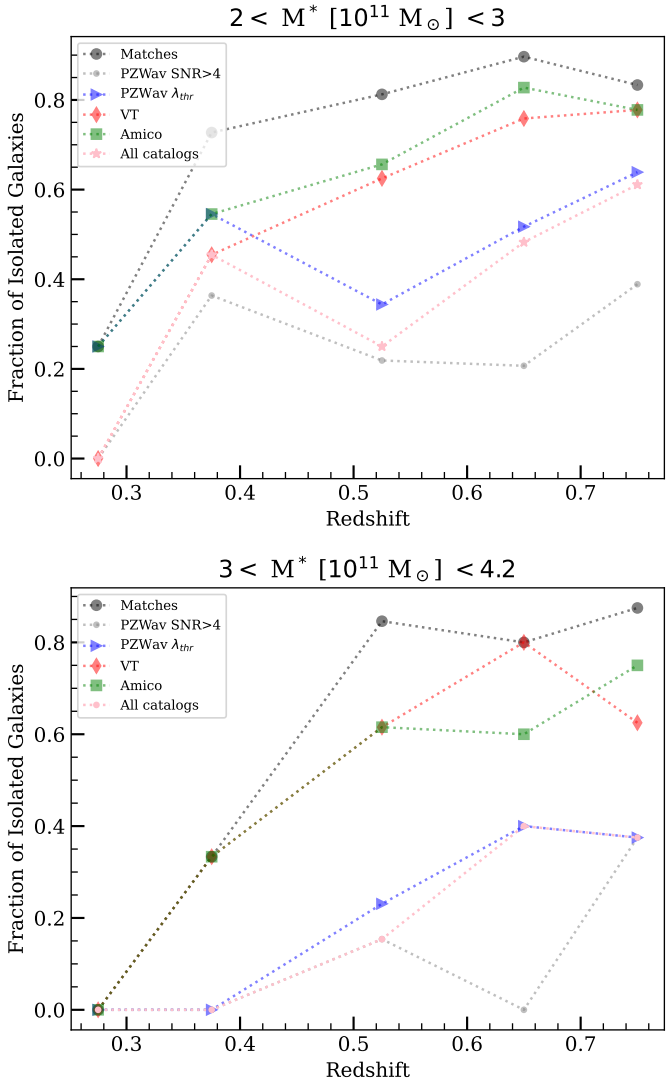

Fig. 10. Evolution of the fraction of galaxies without any cluster association with redshift for two mass ranges: $2 < M^{\star}\,[10^{11}\,M_{\odot}] < 3$ and $3 < M^{\star}\,[10^{11}\,M_{\odot}] < 4.2$, with corresponding halo masses from 1.4 to $4.1 \times 10^{13}\,M_{\odot}$ and 0.41 to $1.4 \times 10^{14}\,M_{\odot}$. In black are the common matches between optical catalogues. The grey colour shows the PZWav complete sample, blue is PZWav after richness selection, red is VT, green is AMICO, and pink is the contribution of all (PZWav subsample) optical catalogues together.

It is important to note that the recovery fraction and association rates may vary depending on the specific criteria and matching procedures employed in the analysis. However, this analysis provides valuable insights into galaxy clustering properties and spatial distribution within the studied redshift range.

6. Summary and conclusions

We conducted a detailed analysis using the PZWav algorithm on the miniJPAS survey, which serves as a precursor to the larger, ongoing J-PAS survey. To enhance our analysis, we utilised an adaptive membership estimator (AME), which improved the characterisation of the cluster candidates. The key findings of this study are as follows:

– The PZWav catalogue is composed of 574 cluster candidates within $0.05 < z < 0.8$ at $S/N > 4$.

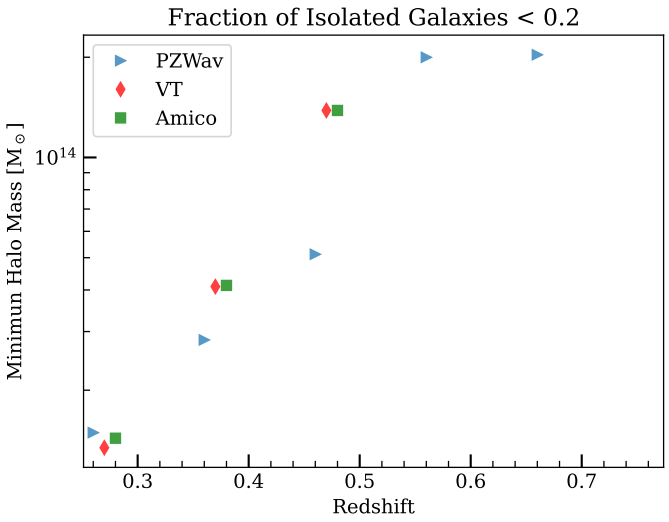

Fig. 11. Minimum halo mass in the function of redshift for ensuring a fraction of isolated galaxies lower than 0.2. With blue triangles, we show PZWav $\lambda > \lambda_{\rm thr}$; VT is indicated with red diamonds; and in green are the AMICO values. Halo masses were estimated following the $M^\star - M_{\rm h}$ relation described in Gozaliasl et al. (2018). The mean redshift values have been artificially displaced for better visualisation.

- Defining different absolute magnitude limits allowed us to better characterise the systems in terms of richness, optical luminosity, and stellar mass. We applied $M_r < -19.5$ at low redshift ($z < 0.3$, group regime) and $M_r < -21.25$ for high redshift ($0.3 < z < 0.8$, cluster regime).
- Applying a richness selection method (limits of 1.9 and 3.0 for cluster and group regimes) resulted in a subset of 221 candidates.
- Making use of the AME, we could calculate optical proxies for scaling relations, such as richness, optical luminosity, and stellar mass, weighted by the galaxy membership probability. Scaling relations using PZWav results revealed intrinsic scatter of $\sigma_{\log_{10}(M|\mathcal{R})} = 0.039 \pm 0.016$; $\sigma_{\log_{10}(M|L_\lambda)} = 0.076 \pm 0.019$; and $\sigma_{\log_{10}(M|M^\star_\lambda)} = 0.080 \pm 0.021$.
- The overlapping miniJPAS area with the AEGIS X-ray survey revealed 17 X-ray sources with an optical counterpart. Among them, we recovered a structure of $M_{200} = (3.75 \pm 0.5) \times 10^{13}\ M_\odot$ at $z = 0.745$. Reanalysing the data with the optical centres detected by PZWav as the reference, we generated a new X-ray catalogue with 37 clusters. Of these, 20 are new detections.
- Matching the cluster catalogue of the different optical cluster finders (PZWav, AMICO, and VT) revealed 43 common identifications. The redshift and centre offsets are within 0.001 and 0.10 Mpc, respectively.
- Statistics revealed notable differences between the properties of matched and non-matched galaxy clusters. The median values of mass proxies are consistently higher for the matched clusters, indicating their higher probability of being a true detection.
- The analysis of the fraction of isolated galaxies provided a prediction of the catalogue significance. For low-mass halos, $f \sim 40\%$, while higher mass halos present $f \sim 30\%$.

We conclude that alongside AMICO and VT, PZWav demonstrates strong performance in detecting galaxy clusters through the utilisation of the PDF of photometric redshifts. The ability to detect low-mass structures at high redshifts highlights the depth of the survey. This preliminary analysis, along with other studies focusing on the miniJPAS survey, shows the potential of the J-PAS survey, including down to group scales.

Acknowledgements. Based on observations made with the JST250 telescope and PathFinder camera for the miniJPAS project at the Observatorio Astrofísico de Javalambre (OAJ), in Teruel, owned, managed, and operated by the Centro de Estudios de Física del Cosmos de Aragón (CEFCA). We acknowledge the OAJ Data Processing and Archiving Unit (UPAD) for reducing and calibrating the OAJ data used in this work. Funding for OAJ, UPAD, and CEFCA has been provided by the Governments of Spain and Aragón through the Fondo de Inversiones de Teruel; the Aragón Government through the Research Groups E96, E103, E16_17R, and E16_20R; the Spanish Ministry of Science, Innovation and Universities (MCIU/AEI/FEDER, UE) with grant PGC2018-097585-B-C21; the Spanish Ministry of Economy and Competitiveness (MINECO/FEDER, UE) under AYA2015-66211-C2-1-P, AYA2015-66211-C2-2, AYA2012-30789, and ICTS-2009-14; and European FEDER funding (FCDD10-4E-867, FCDD13-4E-2685). This work made use of the computing facilities of the Laboratory of Astroinformatics (IAG/USP, NAT/Unicsul), whose purchase was made possible by the Brazilian agency FAPESP (grant 2009/54006-4) and the INCT-A. L.D. acknowledges the support from the scholarship from the Brazilian federal funding agency Coordenação de Aperfeiçoamento de Pessoal de Nível Superior – Brasil (CAPES). E.S.C. acknowledges the support of the funding agencies CNPq (#309850/2021-5) and FAPESP (#2023/02709-9). P.A.A.L. thanks the support of CNPq (grants 433938/2018-8 and 312460/2021-0) and FAPERJ (grant E-26/200.545/2023). R.G.D. acknowledges financial support from the State Agency for Research of the Spanish MCIU through the "Center of Excellence Severo Ochoa" award to the Instituto de Astrofísica de Andalucía, CEX2021-001131-S, funded by MCIN/AEI/10.13039/501100011033, and to financial support from the projects PID-2019-109067-GB100 and PID2022-141755NB-I00. R.A.D. acknowledges support from the Conselho Nacional de Desenvolvimento Científico e Tecnológico – CNPq through BP grant 308105/2018-4, and the Financiadora de Estudos e Projetos – FINEP grants REF. 1217/13 – 01.13.0279.00 and REF 0859/10 – 01.10.0663.00 and also FAPERJ PRONEX grant E-26/110.566/2010 for hardware funding support for the JPAS project through the National Observatory of Brazil and Centro Brasileiro de Pesquisas Físicas. L.M. acknowledges support from the grants PRIN-MIUR 2017 WSCC32 and ASI n.2018-23-HH.0. S.B. acknowledges support from the Spanish Ministerio de Ciencia e Innovación through project PGC2018-097585-B-C22 and the Generalitat Valenciana project PROMETEO/2020/085. This paper has gone through internal review by the J-PAS collaboration. We would like to thank the internal referees Adi Zitrin and Carlos Hernández-Monteagudo for their helpful comments and suggestions.

References

Allen, S. W., Evrard, A. E., & Mantz, A. B. 2011, ARA&A, 49, 409
Arnouts, S., & Ilbert, O. 2011, Astrophysics Source Code Library [record ascl:1108.009]
Bellagamba, F., Sereno, M., Roncarelli, M., et al. 2019, MNRAS, 484, 1598
Benitez, N., Dupke, R., Moles, M., et al. 2014, arXiv e-prints [arXiv:1403.5237]
Bonoli, S., Marín-Franch, A., Varela, J., et al. 2021, A&A, 653, A31
Campello, R. J. G. B., Moulavi, D., & Sander, J. 2013, in Advances in Knowledge Discovery and Data Mining, eds. J. Pei, V. S. Tseng, L. Cao, H. Motoda, & G. Xu (Berlin, Heidelberg: Springer-Verlag), 160
Carlberg, R. G., Yee, H. K. C., Ellingson, E., et al. 1996, ApJ, 462, 32
Cenarro, A. J., Moles, M., Cristóbal-Hornillos, D., et al. 2019, A&A, 622, A176
Costanzi, M., Rozo, E., Simet, M., et al. 2019, MNRAS, 488, 4779
Davis, M., Guhathakurta, P., Konidaris, N. P., et al. 2007, ApJ, 660, L1
de Jong, J. T. A., Verdoes Kleijn, G. A., Kuijken, K. H., & Valentijn, E. A. 2013, Exp. Astron., 35, 25
Doroshkevich, A. G., Gottlober, S., & Madsen, S. 1997, A&AS, 123, 495
Doubrawa, L., Cypriano, E. S., Finoguenov, A., et al. 2023, MNRAS, 526, 4285
Dvorkin, I., & Rephaeli, Y. 2015, MNRAS, 450, 896
Ebeling, H., & Wiedenmann, G. 1993, Phys. Rev. E, 47, 704
El-Ad, H., Piran, T., & da Costa, L. N. 1996, ApJ, 462, L13
Erfanianfar, G., Finoguenov, A., Tanaka, M., et al. 2013, ApJ, 765, 117
Ettori, S., Morandi, A., Tozzi, P., et al. 2009, A&A, 501, 61
Euclid Collaboration (Adam, R., et al.) 2019, A&A, 627, A23
Euclid Collaboration (Scaramella, R., et al.) 2022, A&A, 662, A112
Evrard, A. E. 1997, MNRAS, 292, 289
Gal, R. R. 2006, arXiv e-prints [arXiv:astro-ph/0601195]
Giocoli, C., Marulli, F., Moscardini, L., et al. 2021, A&A, 653, A19
Gladders, M. D., & Yee, H. K. C. 2005, ApJS, 157, 1
Gonzalez, A. 2014, Building the Euclid Cluster Survey – Scientific Program, 7
González Delgado, R. M., Díaz-García, L. A., de Amorim, A., et al. 2021, A&A, 649, A79

González Delgado, R. M., Rodríguez-Martín, J. E., Díaz-García, L. A., et al. 2022, A&A, 666, A84
Gozaliasl, G., Finoguenov, A., Khosroshahi, H. G., et al. 2018, MNRAS, 475, 2787
Hernán-Caballero, A., Varela, J., López-Sanjuan, C., et al. 2021, A&A, 654, A101
Hsieh, B. C., Yee, H. K. C., Lin, H., & Gladders, M. D. 2005, ApJS, 158, 161
Ider Chitham, J., Comparat, J., Finoguenov, A., et al. 2020, MNRAS, 499, 4768
Ikeuchi, S., & Turner, E. L. 1991, MNRAS, 250, 519
Kelly, B. C. 2007, ApJ, 665, 1489
Kiang, T. 1966, Z. Astrophys., 64, 433
Kim, R. S. J., Kepner, J. V., Postman, M., et al. 2002, AJ, 123, 20
Klein, M., Mohr, J. J., Desai, S., et al. 2017, MNRAS, 474, 3324
Laur, J., Tempel, E., Tamm, A., et al. 2022, A&A, 668, A8
Le Fèvre, O., Vettolani, G., Garilli, B., et al. 2005, A&A, 439, 845
Leauthaud, A., Finoguenov, A., Kneib, J.-P., et al. 2010, ApJ, 709, 97
Leauthaud, A., George, M. R., Behroozi, P. S., et al. 2012a, ApJ, 746, 95
Leauthaud, A., Tinker, J., Bundy, K., et al. 2012b, ApJ, 744, 159
Lesci, G. F., Nanni, L., Marulli, F., et al. 2022a, A&A, 665, A100
Lesci, G. F., Marulli, F., Moscardini, L., et al. 2022b, A&A, 659, A88
Li, C., & White, S. D. M. 2009, MNRAS, 398, 2177
Lopes, P. A. A., de Carvalho, R. R., Gal, R. R., et al. 2004, AJ, 128, 1017
Martí, P., Miquel, R., Castander, F. J., et al. 2014, MNRAS, 442, 92
Maturi, M., Bellagamba, F., Radovich, M., et al. 2019, MNRAS, 485, 498
Maturi, M., Finoguenov, A., Lopes, P. A. A., et al. 2023, A&A, 678, A145
Mendes de Oliveira, C., Ribeiro, T., Schoenell, W., et al. 2019, MNRAS, 489, 241
Merloni, A., Predehl, P., Becker, W., et al. 2012, arXiv e-prints [arXiv:1209.3114]
Pacaud, F., Clerc, N., Giles, P. A., et al. 2016, A&A, 592, A2
Parroni, C., Mei, S., Erben, T., et al. 2017, ApJ, 848, 114
Planck Collaboration XIII. 2016, A&A, 594, A13
Ramella, M., Boschin, W., Fadda, D., & Nonino, M. 2001, A&A, 368, 776
Reiprich, T. H., & Böhringer, H. 2002, ApJ, 567, 716
Rodríguez-Martín, J. E., González Delgado, R. M., Martínez-Solaeche, G., et al. 2022, A&A, 666, A160
Rykoff, E. S., Rozo, E., Busha, M. T., et al. 2014, ApJ, 785, 104
Shewchuk, J. R. 1996, in Applied Computational Geometry Towards Geometric Engineering, eds. M. C. Lin, & D. Manocha (Berlin, Heidelberg: Springer-Verlag), 203
Soares-Santos, M., de Carvalho, R. R., Annis, J., et al. 2011, ApJ, 727, 45
Sommer, M. W., Schrabback, T., Applegate, D. E., et al. 2022, MNRAS, 509, 1127
The Dark Energy Survey Collaboration 2005, arXiv e-prints [arXiv:astro-ph/0510346]
Voit, G. M. 2005, Rev. Mod. Phys., 77, 207
Weinberg, D. H., Mortonson, M. J., Eisenstein, D. J., et al. 2013, Phys. Rep., 530, 87
Werner, S. V., Cypriano, E. S., Gonzalez, A. H., et al. 2023, MNRAS, 519, 2630
Willmer, C. N. A. 2018, ApJS, 236, 47
Zaninetti, L. 1995, A&AS, 109, 71
Zheng, Y.-L., & Shen, S.-Y. 2021, ApJ, 911, 105

[1] Department of Physics, University of Helsinki, PO Box 64, 00014 Helsinki, Finland
[2] Departamento de Astronomia, Instituto de Astronomia, Geofísica e Ciências Atmosféricas da USP, Cidade Universitária, 05508-900 São Paulo, SP, Brazil
e-mail: lia.doubrawa@usp.br
[3] Observatório do Valongo, Universidade Federal do Rio de Janeiro, Ladeira do Pedro Antônio 43, Rio de Janeiro, RJ 20080-090, Brazil
[4] Department of Astronomy, University of Florida, Gainesville, FL 32611-2055, USA
[5] Zentrum für Astronomie, Universitatät Heidelberg, Philosophenweg 12, 69120 Heidelberg, Germany
[6] Institute for Theoretical Physics, Philosophenweg 16, 69120 Heidelberg, Germany
[7] Observatório Nacional, Rua General José Cristino, 77, São Cristóvão, 20921-400 Rio de Janeiro, RJ, Brazil
[8] Department of Astronomy, University of Michigan, 311 West Hall, 1085 South University Ave., Ann Arbor, USA
[9] Department of Physics and Astronomy, University of Alabama, Box 870324, Tuscaloosa, AL, USA
[10] Instituto de Astrofísica de Andalucía (IAA-CSIC), Glorieta de la Astronomía s/n, 18008 Granada, Spain
[11] Departamento de Física Matemática, Instituto de Física, Universidade de São Paulo, Rua do Matão, 1371, 05508-090 São Paulo, Brazil
[12] Centro de Estudios de Física del Cosmos de Aragón (CEFCA), Unidad Asociada al CSIC, Plaza San Juan, 1, 44001 Teruel, Spain
[13] Donostia International Physics Center (DIPC), Manuel Lardizabal Ibilbidea, 4, San Sebastián, Spain
[14] Ikerbasque, Basque Foundation for Science, 48013 Bilbao, Spain
[15] Instituto de Física, Universidade Federal da Bahia, 40210-340 Salvador, BA, Brazil
[16] Instruments4, 4121 Pembury Place, La Canada Flintridge, CA 91011, USA

Appendix A: X-ray catalogue

In Sec. 5.2 we presented details about the produced extended X-ray catalogue based on the PZWav optical detection catalogue. In Table A.1, we present the counterpart catalogue of 37 X-rays within the redshift range of $0.55 < z < 0.8$. We list the cluster identification number from the optical catalogue (ID); the sky coordinates (RA, DEC); the optical redshift estimate (z); the obtained flux and estimated error (Flux, eFlux); the X-ray luminosity and error (Lx, eLx); mass estimates; and the corresponding uncertainties obtained from Lx-Mass scaling relations from Leauthaud et al. (2012b) (M200c, eM200c).

Table A.1. Extended X-ray catalogue based on the PZWav optical centres. The rows are sorted by M_{200c}.

ID	RA	DEC	z	Flux	eFlux	Lx	eLx	M200c	eM200c
16	213.80150	52.09198	0.070	1.05e-14	8.06e-15	2.15e+41	1.64e+41	7.22e+12	3.16e+12
11	214.98826	53.11720	0.201	1.92e-15	6.34e-16	3.85e+41	1.27e+41	9.39e+12	1.88e+12
20	214.33039	52.59097	0.238	1.77e-15	4.35e-16	5.20e+41	1.27e+41	1.10e+13	1.66e+12
153	213.89208	52.19922	0.432	8.04e-16	5.34e-16	1.01e+42	6.74e+41	1.41e+13	5.44e+12
79	215.00479	53.10381	0.360	1.45e-15	3.58e-16	1.11e+42	2.73e+41	1.60e+13	2.42e+12
33	214.63203	52.46455	0.280	2.47e-15	5.56e-16	1.01e+42	2.28e+41	1.62e+13	2.25e+12
270	214.26067	52.37080	0.531	6.70e-16	3.26e-16	1.49e+42	7.30e+41	1.64e+13	4.75e+12
103	215.00902	52.97046	0.452	1.01e-15	2.70e-16	1.39e+42	3.74e+41	1.69e+13	2.78e+12
122	214.33778	52.24765	0.290	2.74e-15	7.69e-16	1.21e+42	3.41e+41	1.80e+13	3.10e+12
115	214.18501	52.28390	0.374	1.66e-15	5.37e-16	1.37e+42	4.46e+41	1.81e+13	3.56e+12
219	213.91066	52.04932	0.426	1.41e-15	6.12e-16	1.64e+42	7.10e+41	1.93e+13	4.99e+12
9	214.51725	52.38455	0.434	2.14e-15	5.68e-16	2.54e+42	6.76e+41	2.53e+13	4.12e+12
81	214.44518	52.73449	0.620	1.08e-15	3.25e-16	3.41e+42	1.02e+42	2.55e+13	4.68e+12
113	213.93670	52.12280	0.586	1.31e-15	6.33e-16	3.51e+42	1.69e+42	2.69e+13	7.70e+12
499	214.50621	52.45121	0.758	8.23e-16	2.55e-16	4.63e+42	1.43e+42	2.71e+13	5.12e+12
241	213.69214	52.13455	0.698	9.62e-16	6.23e-16	4.27e+42	2.76e+42	2.73e+13	1.02e+13
198	214.36356	52.54103	0.481	2.34e-15	3.65e-16	3.62e+42	5.63e+41	3.03e+13	2.94e+12
56	213.57773	52.15029	0.390	3.64e-15	1.06e-15	3.27e+42	9.55e+41	3.10e+13	5.53e+12
133	214.76357	52.52109	0.436	3.35e-15	1.35e-15	3.97e+42	1.61e+42	3.36e+13	8.18e+12
151	214.83700	52.89762	0.752	1.32e-15	3.07e-16	6.72e+42	1.56e+42	3.46e+13	4.94e+12
108	214.48984	52.43453	0.686	1.63e-15	4.31e-16	6.39e+42	1.68e+42	3.57e+13	5.78e+12
230	213.95265	52.14622	0.624	1.97e-15	1.04e-15	5.97e+42	3.16e+42	3.64e+13	1.13e+13
87	215.58267	53.36040	0.636	1.91e-15	6.36e-16	6.09e+42	2.02e+42	3.64e+13	7.33e+12
3	214.47856	52.58452	0.680	1.89e-15	2.98e-16	7.16e+42	1.12e+42	3.87e+13	3.79e+12
46	214.76543	52.96109	0.654	2.06e-15	3.24e-16	7.00e+42	1.09e+42	3.91e+13	3.82e+12
332	214.08193	52.24351	0.576	2.56e-15	5.39e-16	6.23e+42	1.30e+42	3.92e+13	5.08e+12
99	215.41558	53.38501	0.628	2.68e-15	7.74e-16	8.06e+42	2.32e+42	4.39e+13	7.74e+12
273	214.94426	53.16735	0.150	4.20e-14	1.56e-14	4.08e+42	1.51e+42	4.44e+13	9.96e+12
97	214.79143	52.61771	0.563	4.01e-15	4.08e-16	9.00e+42	9.17e+41	5.02e+13	3.21e+12
492	215.44998	52.87806	0.420	6.84e-15	1.68e-15	7.32e+42	1.80e+42	5.05e+13	7.64e+12
7	213.31492	52.22110	0.498	5.48e-15	2.15e-15	8.98e+42	3.53e+42	5.34e+13	1.26e+13
35	215.66653	53.36300	0.776	2.87e-15	8.78e-16	1.44e+43	4.43e+42	5.52e+13	1.03e+13
13	215.75333	53.26884	0.697	3.84e-15	1.45e-15	1.45e+43	5.49e+42	5.98e+13	1.36e+13
23	215.14407	53.13991	0.736	3.55e-15	4.18e-16	1.54e+43	1.81e+42	5.98e+13	4.41e+12
550	215.37229	53.46197	0.680	4.76e-15	1.35e-15	1.67e+43	4.74e+42	6.66e+13	1.15e+13
140	214.97817	53.22724	0.406	2.04e-14	6.35e-15	1.95e+43	6.09e+42	9.61e+13	1.82e+13
1	213.61502	51.93392	0.287	5.10e-14	5.11e-15	2.15e+43	2.16e+42	1.14e+14	7.21e+12